Nonlinear Observer for Tightly Coupled Integrated Inertial Navigation Aided by RTK-GNSS Measurements

Jakob M. Hansen[1], Tor Arne Johansen[1], Nadezda Sokolova[1] and Thor I. Fossen[1]

***Abstract*— A modular nonlinear observer is considered for tightly coupled integration of inertial measurements with global satellite measurements. A real-time-kinematic approach is utilized where the rover and base station measure pseudoranges, carrier phase, and carrier phase derived Doppler, to be used in a dual receiver configuration. The modular observer design consists of a nonlinear attitude observer and a translational motion observer. The attitude observer represents the vehicle attitude as unit quaternions and estimates the gyro bias. A translational motion observer based on the double-differenced measurements between the rover and base station receiver is proposed. The ambiguities introduced by the carrier-phase measurements are included in the state vector and are initially considered real valued, later to be resolved to integer values. The advantages of the nonlinear observer compared to a Kalman filter are; reduced computational load, no linearization requirement of the model and proven stability. The proposed observer is verified using experimental data from flights with an unmanned aerial vehicle (UAV), where the position estimates are shown to be within 2-4 centimetres of a GPS L_1 based real-time-kinematic reference solution.**

I. Introduction

Integrating measurements from an inertial measurement unit (IMU) with global navigation satellite system (GNSS) measurements is a common method for estimation of position, linear velocity and attitude (PVA) of a vehicle. The most common integration scheme is the loosely-coupled approach where inertial measurements are integrated with GNSS position and velocity estimates. The position and velocity estimates used in a loosely-coupled system are supplied by a GNSS receiver, where the navigation solution is determined by an integration algorithm, most typically a Kalman filter. Due to the unknown tuning of the filter in the GNSS receiver it can be preferred to use the measurements from the satellites directly in navigation systems to optimize its performance. A tightly-coupled integration scheme can be utilized where inertial measurements are integrated with pseudorange, carrier-phase and Doppler measurements, thereby correcting the state estimates using measurements in the range domain rather than in the position domain. In general tightly-coupled systems have higher performance than loosely-coupled systems as a higher level of control of the nuisance and noise terms can be accounted for. A further advantage of the tightly-coupled system is that aiding from even a few satellites can be used, whereas for loosely-coupled systems at least four satellites must be available for position determination in the receiver. Moreover, at least four satellites are required for obtaining aiding information in loosely-coupled systems, whereas tightly-coupled systems can offer partial aiding with fewer satellites. This increases the robustness of tightly-coupled solutions to satellite signal obstruction.

Tightly-coupled multi-sensor systems using filters, such as the Extended Kalman Filter (EKF), have been subject of extensive research, see [1] and [2]. In [3] enhancements for a tightly-coupled integration on small unmanned vehicles (UAVs) are presented. A low-cost GNSS/IMU integration using a Micro-Electro-Mechanical System (MEMS) IMU with a nonlinear KF approach is developed in [4], while [5] considers a tightly coupled integration using a Kalman filter for accurate mapping using an aerial platform. A comparative study of loosely, tightly and ultra-tightly coupled systems was investigated by [6] using a wide range of inertial sensor grades, and the GIGET tool.

Higher accuracy can be achieved by taking atmospheric disturbances into account, such as ionospheric and tropospheric delay of the satellite signal. These disturbances can, to some extend, be modelled in nominal conditions, or mitigated by using dual or multi-frequency GNSS receivers. Multi-frequency receivers facilitate estimation and compensation of the ionospheric delay, see [2, Section 8.6] or [7]. However, for low-cost applications the high cost of the necessary receiver front-ends presently prevents wide applicability of multi-frequency systems. Furthermore, multi-frequency receivers and antennas often require more space when mounted and can therefore limit their inclusion in constrained applications such as unmanned aerial vehicles (UAVs).

Inclusion of the carrier-phase measurement allows for achieving higher accuracy if the introduced integer ambiguities can be resolved. In [8] a low-cost multiple GNSS antenna configuration is utilized to aid in the ambiguity resolution performed. Multiple approaches for estimation of the integer ambiguities have been studied, e.g. [9], [10], [11] proposing the widely used LAMBDA method, or [12] where a computationally efficient method was proposed using a common-position-shift approach. In [13] an approach using an aiding INS to resolve the ambiguities was investigated, while [14] proposes a near-real-time method based on measurements from multiple epochs. Another method is the real-time-kinematic (RTK) solution where a dual-receiver configuration with a stationary base station and a static or moving rover (i.e. a vehicle) is used. The base station broadcasts its satellite measurements to the rover, which in

[1]Department of Engineering Cybernetics, Norwegian University of Science and Technology, 7491 Trondheim, Norway (e-mail: contact@jmahler.dk, tor.arne.johansen@itk.ntnu.no, nadia.sokolova@sintef.no, thor.fossen@ntnu.no).

turn performs differencing of the measurements for use in the navigation system. With a known base station position precise positioning of the rover is possible. It is also possible to utilize a moving base station: if the base station position is always known the precision can be retained, otherwise inertial sensors might be added to the base station to offer similar state estimation as for the rover. The RTK solution operates under the assumption that the separation between the rover and base station (called the baseline) is short such that the atmospheric signal delays observed by the two receivers are similar. In [15] and [16] a low-cost open source RTK solution is developed. Some environments can decrease the accuracy of the acquired solution due to satellite blockage, which is the topic of [17] where Doppler measurements are used to aid in the RTK computations. Multipath caused by reflected satellite signals can also cause errors in the pseudorange and carrier-phase measurements, but can to some extent be remedied, e.g. by the proposed method of [18]. In [19] the time differenced carrier-phase measurements are used instead of delta-range measurements in a tightly-coupled single receiver system, showing improvements to velocity and attitude estimation, while introduction of a base station was encouraged to obtain centimetre accuracy. Other approaches include the precise point positioning (PPP), see e.g. [20], or differential GNSS, see e.g. [21], which can give results with precision similar to RTK systems. In [22] a tightly-coupled Kalman filter is proposed for a low-cost sensors solution, where the single-differenced ambiguities are included in the state vector, and the Kalman filter solution is verified using automotive experimental data.

When low-cost sensors are used, care should be taken to avoid long time periods of satellite obstruction, as the quality of the inertial sensors will introduce fast diverging state estimates. The measurement noise levels will be higher for low-cost sensors, which will introduce large output noise and might prevent correct resolution of the phase ambiguities.

Applications for tightly-coupled RTK GNSS/INS integration are many and varied. Here the focus will be on UAVs where the applications could include automated landing. UAVs can be landed in vertically placed nets at landing sites or on ships, which require high precision. This paper will focus on a low-cost solution for UAV flights close to an area of interest equipped with a stationary base station.

Previously only loosely-coupled GNSS/INS nonlinear observers have been proposed, leaving the EKF based observers to dominate the field of tight integration. However, recently nonlinear observers have gained interest for tightly-coupled GNSS/INS integration e.g. [23], [24], [25], [26], where long baseline configurations have been considered. Nonlinear observers have some advantages compared to Kalman filters such as; proven stability results for nonlinear systems, no need for linearization of the kinematic model, and lower computational load as shown in e.g. [27] where a tightly coupled nonlinear observer was shown to constitute only around 25% of a comparable multiplicative extended Kalman filter implementation.

A modular observer structure will be considered here, consisting of the nonlinear attitude estimator proposed in [28] and a translational motion observer. The observer structure is based on results by [29] and [30].

This paper is an extension of the work by [27], and [31], here proposing a translational motion observer for estimation of position, linear velocity, and integer ambiguities. The injection terms for the observer are the errors between estimated and measured double-differenced (DD) pseudorange, carrier phase and carrier phase derived Doppler measurements. The method can be implemented using low cost sensors such as MEMS-based inertial sensors and single frequency GNSS receivers. The current paper offers two main contributions to the previous work of the authors:

Time Derivative of Carrier Phase Measurements: An additional aiding measurement is considered, and the observers have been expanded to include the time derivative of the carrier-phase measurement. This measurement can be utilized for injection terms in the double-differenced observer, and require determination of satellite velocity. The time derivative of the carrier phase measurement is used rather than the raw Doppler measurement, due to the lower measurement noise.

Experimental Verification: The proposed observer has been experimentally verified by data acquired using a fixed-wing UAV equipped with a low-cost sensor suite consisting of an ADIS-16488 IMU and a u-Blox LEA-6T GPS L_1 receiver. A second u-Blox receiver of the same model was used as the base station. The reference was determined with an open source RTK solution using the same receiver pair.

A. Notation and Preliminaries

A column vector $x \in \mathbb{R}^3$ is denoted $x := [x_1; x_2; x_3]$ with transpose $x^\intercal$ and vector norm $\|x\|_2$. The skew-symmetric matrix of a vector x is given as:

$$S(x) := \begin{bmatrix} 0 & -x_3 & x_2 \\ x_3 & 0 & -x_1 \\ -x_2 & x_1 & 0 \end{bmatrix}.$$

A unit quaternion, $q = [r_q; s_q]$, is described as consisting of a real part, $r_q \in \mathbb{R}$, and a vector part, $s_q \in \mathbb{R}^3$, where $\|q\|_2 = 1$. A vector $x \in \mathbb{R}^3$ can be represented as a quaternion with zero real part; $\bar{x} = [0; x]$. The product of two quaternions q_1 and q_2 is the Hamiltonian product denoted $q_1 \otimes q_2$.

Superscripts will be used to signify which coordinate frame a vector is decomposed in. Rotation between the frames may be represented by a quaternion, q_a^c, describing the rotation from coordinate frame a to c, with the corresponding rotation matrix $R(q_a^c) \in SO_3$. Various coordinate frames will be used, where the Earth-Centered-Earth-Fixed frame is denoted with e, while b will be used for Body-frame with n denoting the North-East-Down frame. The Earth-Centered-Inertial frame will be denoted with i and will only be used for angular rates, such as the Earth rotation rate; ω_{ie}^e, as the i will later be used to signify signals from the ith satellite.

II. Problem Formulation

A dual receiver configuration consisting of a moving rover and a stationary base station, each equipped with a GNSS receiver, is considered. The base station measures pseudorange, carrier phase and carrier phase derived Doppler and transmits these to the rover for processing, followed by position and velocity estimation. The rover will in addition be equipped with inertial sensors providing specific force and angular rate measurements.

The objective is to estimate position, linear velocity and attitude (PVA) of a moving vehicle by tightly-coupled integration of mentioned measurements. Estimation of the rover PVA as well as the baseline, i.e. the vector (displacement) between rover and base station, are of interest.

The kinematic strapdown equations of the rover are given as:

$$\dot{p}_r^e = v_r^e, \tag{1}$$

$$\dot{v}_r^e = -2S(\omega_{ie}^e)v_r^e + f^e + g^e(p_r^e), \tag{2}$$

$$\dot{q}_b^e = \frac{1}{2}q_b^e \otimes \overline{\omega}_{ib}^b - \frac{1}{2}\overline{\omega}_{ie}^e \otimes q_b^e, \tag{3}$$

where the position, linear velocity and attitude of the rover are described by p_r^e, v_r^e and q_b^e, respectively. The Earth rotation rate in ECEF with respect to ECI decomposed in the ECEF frame is denoted ω_{ie}^e, and is a known constant. The effect of the Earth rotation will be very small compared to the other terms of (2), and can often be disregarded during implementation. However, here it will be included for completeness. The rotation rate ω_{ib}^b describes the Body rotation rate with respect to the ECI frame. The specific force is given by f^e while $g^e(p_r^e)$ specify the position dependent plumb-bob gravity vector. The base station is assumed to be stationary; $\dot{p}_s^e = 0$.

A. Measurement Assumptions

It is assumed that the rover is equipped with an Inertial Measurement Unit (IMU), a GNSS receiver and a magnetometer. The following assumptions on the measurements are made:

Assumption 1: Specific force measurements are available as $f_{\text{IMU}}^b = f^b$.

Remark 1: The accelerometer bias estimation module in [32] and [33] can be added as a first stage providing a bias-compensated acceleration measurement in cascade with the proposed observer. Since this is a cascade, this module has no impact on stability of the error dynamics.

Assumption 2: The rotational rate of a gyro is measured as $\omega_{ib,\text{IMU}}^b = \omega_{ib}^b + b^b$. The gyro bias, $b^b \in \mathbb{R}^3$ is assumed to be slowly time-varying, $\dot{b}^b = 0$, satisfying $\|b^b\|_2 \leq M_b$ for a known bound M_b.

Assumption 3: a magnetometer measures the magnetic field vector at the rover, $m_{\text{MAG}}^b = m^b$, while the position dependent Earth magnetic field m^e in ECEF is assumed known.

Furthermore, the rover and base station are assumed to be equipped with GNSS-receivers measuring; pseudo-range, carrier phase and carrier phase derived Doppler, from at least four common satellites, $m \geq 4$. The satellite positions and velocities are assumed known, which can be satisfied by determination using the broadcast ephemeris data.

The pseudorange and carrier phase measurements at a location p^e transmitted by the ith satellite, see Fig. 1a, can be generalized as:

$$\rho_i = \psi_i + \beta + \gamma_i + \varepsilon_\rho + n_{\rho,i}, \tag{4}$$

$$\lambda\varphi_i = \psi_i + \lambda N_i + \beta + \gamma_i + \varepsilon_\varphi + n_{\varphi,i}, \tag{5}$$

where the pseudo-range and carrier-phase measurements from the ith satellite are denoted ρ_i and φ_i, for $i = 1, 2, \ldots, m$. The geometric range between receiver and satellite is denoted $\psi_i := \|p^e - p_i^e\|_2$, where p_i^e is the satellite position. The carrier-phase integer ambiguity is denoted N_i with signal wavelength λ. The parameters ε_ρ and ε_φ denote the combined orbital, ionospheric and tropospheric delays of the satellite measurements. Furthermore, ε_φ includes antenna induced errors. The $n_\star$ parameters cover individual stochastic errors such as measurement noise and multipath effect. The noise terms have been explicitly included for the aiding measurements to ensure that the measurement noise is not considered cancelled in the differences introduced later. The measurement noise of the aiding measurement will change magnitude when differenced which should be taken into account in the tuning of the observer. The noise terms for the inertial measurements will not be explicitly included as they will not undergo operations that will change their characteristics. All noise sources will be systematically considered in the tuning of the observer. The satellite clock error γ_i can be corrected by applying the clock correction coefficients from the navigation data message. The receiver clock bias, describing the timing difference between receiver and system time, affects all coinciding range measurements similarly, [2, Section 8.4.3]. In the following the clock range bias is treated as a common mode bias, $\beta \in \mathbb{R}$, and is assumed to be slowly time-varying.

The bias is expressed as $\beta = c\Delta_{r,i}$ with $\Delta_{r,i}$ being the receiver clock bias and c being the speed of light. Similarly, the satellite clock error can be expressed as $\gamma_i = c\Delta_{s,i}$ with $\Delta_{s,i}$ being the bias of the ith satellite clock.

Due to large measurement noise, the raw Doppler measurements are usually not included as aiding information. The measurements can either be filtered, which has the drawback of reducing the sample frequency, removing high frequency motion and introduce phase lag, or a substitute can be determined as the time derivative of the carrier-phase measurements. In [34] the carrier phase derived Doppler is obtained by use of a finite impulse response filter, resulting in accurate velocity measurements for a standalone Global Positioning System (GPS) receiver. In the following the time derivative of the carrier-phase will be considered, [35]:

$$\lambda\dot{\varphi}_i = \dot{\psi}_i + \dot{\beta} + \dot{\gamma}_i + \dot{n}_{\varphi,i}, \tag{6}$$

where the ambiguity and multipath terms have been eliminated due to the short time horizon of the derivative.

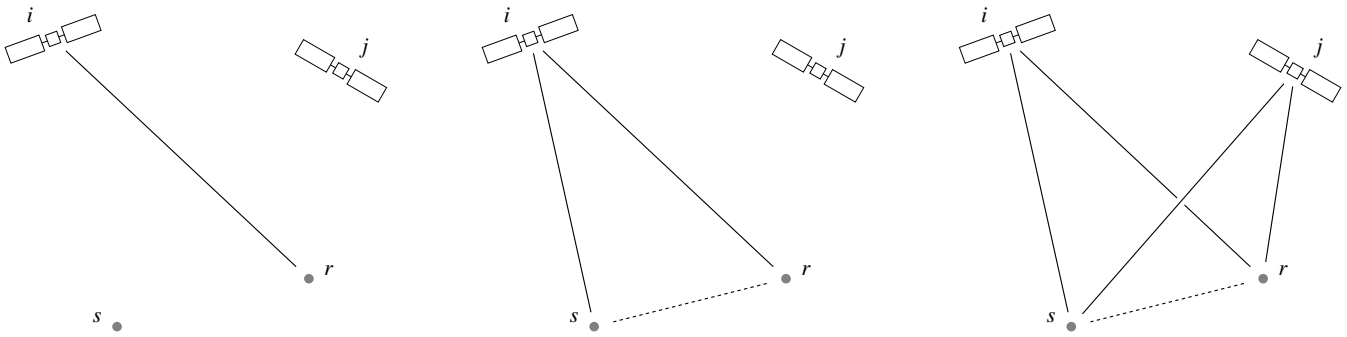

(a) Undifferenced measurements between one receiver and one satellite.

(b) Single-difference measurements between two receivers and one satellite.

(c) Double-difference measurements between two receivers and two satellites.

Fig. 1: GNSS measurements for un-, single- and double-differenced configurations

Furthermore, by assuming constant atmospheric delays over the time interval between consecutive phase measurements these can also be eliminated, where any residual delays will be absorbed by the noise term, [35].

A generalized model for the time derivative of the phase measurement can be expressed as:

$$\lambda \upsilon_i = h_i^{\mathsf{T}} (v^e - v_i^e) + \dot{\beta} + \dot{\gamma}_i + n_{\upsilon,i}, \tag{7}$$

where the satellite velocity is denoted v_i^e, and the line-of-sight vector is; $h_i = (p^e - p_i^e)/\psi_i$. The constructed carrier phase derived measurement is denoted υ_i, while $n_{\upsilon,i}$ describes the stochastic errors.

Remark 2: The carrier-phase measurements, φ, are given in units of cycles, and can be converted to meters by multiplication with the wavelength. The carrier phase derived Doppler measurements, υ, are given in Hertz and can be converted to velocity described in meters per second by multiplication with the wavelength.

Superscripts of r and s will be used to distinguish between the measurements at rover and base station, respectively. These superscripts are not to be confused with the coordinate frame as the satellite measurements will always be given in the ECEF-frame. It is assumed that the rover is sufficiently close to the base station such that the ionospheric and tropospheric delays are spatially correlated between the two receivers and will therefore cancel, i.e. $\varepsilon_\rho^r = \varepsilon_\rho^s$, $\varepsilon_\varphi^r = \varepsilon_\varphi^s$, $\varepsilon_\upsilon^r = \varepsilon_\upsilon^s$. While it is possible to obtain centimetre accuracy of the position estimates with baseline of 20 *km* for resolved ambiguities, see [2, Section 10.2], maintaining high accuracy requires shorter baselines. Short baselines, less than 10 *km*, are preferred to reduce cycle-slips, while for longer baselines the accuracy degrades due to decorrelation of the atmospheric propagation errors. This can be mitigated by use of dual-frequency GNSS measurements and modelling of the troposphere. The atmospheric disturbances can therefore be corrected for by differencing measurements at rover position with measurements at the base station. The GNSS measurement configuration is depicted in Fig. 1b showing two satellites, i and j, and two receivers, r and b, where the baseline is shown as a dashed line. It is vital when differencing measurements that the they are acquired at the same time epoch.

The single-differenced (SD) measurements between rover and base station are given as:

$$\Delta\rho_i = \Delta\psi_i + \Delta\beta + n_{\Delta\rho,i}, \tag{8}$$

$$\lambda\Delta\varphi_i = \Delta\psi_i + \Delta N_i\lambda + \Delta\beta + n_{\Delta\varphi,i}, \tag{9}$$

$$\lambda\Delta\upsilon_i = h_i^{r\mathsf{T}} (v_r^e - v_i^e) + h_i^{s\mathsf{T}} v_i^e + n_{\Delta\upsilon,i}, \tag{10}$$

where $\Delta\rho_i := \rho_i^r - \rho_i^s$, $\Delta\varphi_i := \varphi_i^r - \varphi_i^s$, $\Delta\upsilon_i := \upsilon_i^r - \upsilon_i^s$, $\Delta N_i := N_i^r - N_i^s$, $\Delta\beta := \beta^r - \beta^s$, and $\Delta\psi_i := \psi_i^r - \psi_i^s$ is the geometric baseline between rover and base station. The differenced noise terms are given as; $n_{\Delta\rho,i} := n_{\rho,i}^r - n_{\rho,i}^s$, $n_{\Delta\varphi,i} := n_{\varphi,i}^r - n_{\varphi,i}^s$, and $n_{\Delta\upsilon,i} := n_{\upsilon,i}^r - n_{\upsilon,i}^s$. The normalised line-of-sight vectors h_i^r and h_i^s, between the ith satellite and rover and base station are given as:

$$h_i^r = \frac{p_r^e - p_i^e}{\|p_r^e - p_i^e\|_2}, \qquad h_i^s = \frac{p_s^e - p_i^e}{\|p_s^e - p_i^e\|_2}. \tag{11}$$

From (8) and (9) it is evident that $\Delta\beta$ is the same for all satellites so it can be cancelled by further differencing the measurements this time between satellites. This is typically achieved by selecting the satellite with highest elevation as reference. The double-differenced (DD) measurement principle is depicted in Fig. 1c while the measurement model is given as:

$$\nabla\Delta\rho_{ij} = \nabla\Delta\psi_{ij} + n_{\nabla\Delta\rho,ij}, \tag{12}$$

$$\lambda\nabla\Delta\varphi_{ij} = \nabla\Delta\psi_{ij} + \nabla\Delta N_{ij}\lambda + n_{\nabla\Delta\varphi,ij}, \tag{13}$$

$$\begin{aligned}\lambda\nabla\Delta\upsilon_{ij} = {} & h_j^{r\mathsf{T}} \left(v_r^e - v_j^e\right) - h_i^{r\mathsf{T}} (v_r^e - v_i^e) + h_j^{s\mathsf{T}} v_j^e \\ & - h_i^{s\mathsf{T}} v_i^e + n_{\nabla\Delta\upsilon,ij},\end{aligned} \tag{14}$$

where $\nabla\Delta\rho_{ij} := \Delta\rho_j - \Delta\rho_i$, $\nabla\Delta\varphi_{ij} := \Delta\varphi_j - \Delta\varphi_i$, $\nabla\Delta\upsilon_{ij} := \Delta\upsilon_j - \Delta\upsilon_i$, $\nabla\Delta\psi_{ij} := \Delta\psi_j - \Delta\psi_i$, and $\nabla\Delta N_{ij} := \Delta N_j - \Delta N_i$ with the jth satellite representing the reference satellite. The measurement noise is; $n_{\nabla\Delta\rho,ij} := n_{\Delta\rho,j} - n_{\Delta\rho,i}$, $n_{\nabla\Delta\varphi,ij} := n_{\Delta\varphi,j} - n_{\Delta\varphi,i}$ and $n_{\nabla\Delta\upsilon,ij} := n_{\Delta\upsilon,j} - n_{\Delta\upsilon,i}$.

Due to measurement differencing between satellites, the number of available observations will be $m-1$, where m is the number of tracked satellites. The double-differenced measurements will be used in injection terms of the proposed observer structure. The single-differenced measurements are

not utilized in the observer structure due to the presence of the receiver clock bias.

When differencing GNSS measurements a rule of thumb is that the stochastic error will increase in standard deviation by $\sqrt{2}$, while the systematic errors will decrease, see [36].

III. Noise Analysis

A common assumption of the Extended Kalman filter is that the measurement and process noise are Gaussian. The nonlinear observer structure proposed here does not make any specific assumptions on the distribution of GNSS measurement noise in; (4)–(7), (8)–(10) and (12)–(14), or the inertial measurement noise introduced with the specific force, angular rate and magnetometer measurements. However, when tuning the observer gains it is advantageous to have the knowledge of the noise levels and types. It is therefore desired to investigate the noise distribution and determine the standard deviation of the undifferenced (UD) and double-differenced GNSS measurement noise. The noise type is the same for all types and brands of receivers, whereas the standard deviations are receiver and antenna specific. For the inertial measurement noise industrial data sheets offer accurate noise characteristics. If the noise characteristics cannot be assumed Gaussian white the state space model can be augmented to include colored noise models with white driving noise, see e.g. [2, Section 4.6.3] or [37, Section 7.5]. The following section will therefore only consider the GNSS measurement noise.

Experimental data was collected at 1 Hz, by two identical u-Blox LEA-6T receivers with a baseline of 1 m. The experiment was carried out at latitude 63.4° and longitude 10.5°, Norway, on a rooftop. Some multipath effect is experienced which affect the undifferenced measurements, while it can be mostly mitigated for the double-differenced measurements due to the short baseline. The positions of the receivers were determined by averaging over a 24 hour long data set. Some satellites were occasionally obstructed and the noise levels of the GNSS measurements are therefore found during a time interval with multiple common satellites visible by both receivers. The satellites are commonly visible for $3-6$ hours during good open sky conditions.

In the case of the undifferenced measurements the raw pseudorange, carrier phase and carrier phase derived Doppler measurements are corrected for: time of transmission (the satellite moves during the signal transmission time), atmospheric disturbances, and receiver clock bias (estimated using a Kalman filter). Furthermore, the geometric range from satellite to receiver ψ_i^r and ψ_i^s are computed. The tropospheric delay can be modelled using e.g. [38], whereas the ionospheric delay might be modelled using the Klobuchar model. For the UD noise terms some residual errors will be present due to the imperfection of the applied models. Furthermore, uncertainty of the estimated receiver clock and multipath effects remain.

For the double-differenced measurements the noise terms are found by isolation of $n_\star$ in (12)-(14). Given the short baseline (1 meter), the ionospheric and tropospheric delays are considered to be completely removed, whereas the residual atmospheric effects are negligible such that the noise term only consists of receiver noise and multipath.

The noise estimates of the DD measurements are shown in Fig. 2a–2c, with 6 available satellites; resulting in 5 DD measurements. The noise estimates have been de-trended to remove first order dependencies and initial offset, which is common practice e.g. when determining scintillation effects, see [39] or [40]. The colors indicate measurements from different satellites. The average standard deviations of the estimated measurement noise are presented in Table I, with the noise of the UD measurements for comparison. The standard deviations corresponds well with the results found in [1, Section 9.4.2.4] for an update rate of 1 Hz. Moreover, according to [1, Section 9.4.2.4] the standard deviations might be increased with higher receiver sampling rates.

To obtain a large time window for noise analysis some of the satellites have low elevation at the edges of the time window, this results in an increase in standard deviation, as seen in e.g. the yellow and red graphs in Fig 2c around $9000-10000$ seconds. Nevertheless these satellites have been included to estimate an average standard deviation of the noise terms under various conditions. Similar effects can be seen in [41] where a filter for separation of the multipath components is proposed, while also locating reflecting objects. Short and long baselines are considered in [42] and [43], where undifferenced, single- and double-differenced GNSS signals from several constellations are analysed.

TABLE I: Standard deviations of GNSS measurements.

	UD	DD
Pseudorange, ρ, $[m]$	1.560	1.597
Carrier-phase, φ, $[m]$	0.207	0.020
Derived Doppler, υ, $[m/s]$	0.682	0.055

The double-differenced pseudorange and carrier phase derived Doppler measurements appear almost white, whereas the carrier phase measurements include non-white behaviour. There are two common practices for handling this in observer structures: a) augment the observer to model states for the non-white noise processes, or b) assume a white distribution with larger standard deviation than the actual distribution to over-bound the measurement noise. The over-bounding method was proposed in [44], and used e.g. in [45] where multipath, receiver noise and atmospheric delays were investigated for pseudoranges in a single-differenced configuration. In general the code and phase noise can be represented by over-bounding white noise, even though a Gauss-Markov process is a more suitable model. It might be beneficial to use slightly inflated noise characteristics even when employing Gauss-Markov processes. Additionally, the distributions cannot be expected to be stationary as several factors can cause changes on the fly such as: multipath (especially at the rover), elevation angle, rover dynamics and C/N_0 levels. In conclusion; it might be advantageous to use higher values for the standard deviations when used

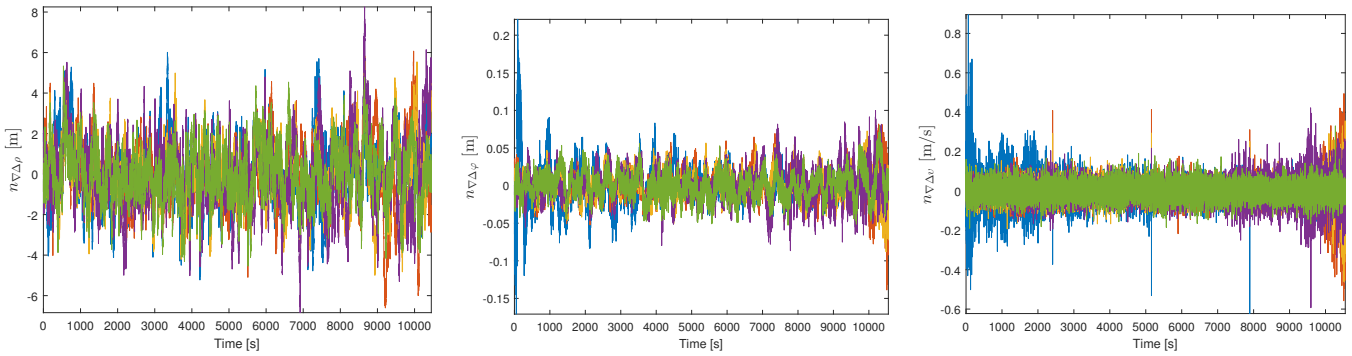

(a) Double-differenced pseudoranges (b) Double-differenced carrier-phase (c) Double-differenced derived Doppler

Fig. 2: Noise analysis of double-differenced GNSS measurements, over a 3 hours period.

for observer tuning to accommodate for imperfect Gaussian white noise behaviour.

IV. Observer Structure

In the following sections a nonlinear observer is proposed based on double-differenced GPS L_1 measurements. A modular observer structure consisting of a nonlinear attitude estimator and a translational motion observer (TMO) is considered. The framework is the same as presented in [27] and [31] although a different TMO is used: here the dual receiver configuration is used leading to differenced measurements, whereas in [27], a single receiver was used to obtain a tightly-coupled navigation solution.

The observer structure, shown in Fig. 3, consists of: two GNSS receivers, IMU, magnetometer (MAG), nonlinear attitude observer, a TMO, and a Riccati solver with a gain estimator. Two feedback loops are present in the structure: the feedback of $\hat{f}^e$ from the TMO to the attitude observer, and a feedback of the estimated rover position and velocity to the computation of gain matrices.

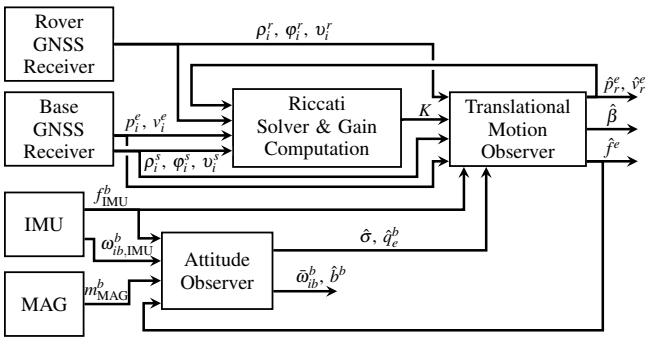

Fig. 3: Block diagram of observer structure.

The GNSS measurements (ρ_i^r, φ_i^r, v_i^r, ρ_i^s, φ_i^s, and v_i^s) are measured by the receivers in the ECEF frame, while the satellite positions and velocities (p_i^e and v_i^e) are computed from the ephemeris data, see [2, Appendix C]. These computations are included in the "Base GNSS Receiver" block for convenience.

Remark 3: The carrier phase derived Doppler measurement is based on the carrier-phase change, and expresses the change in geometric distance and clock drift over a time interval, see [2, Section C.4.2]. The carrier phase derived Doppler measurement therefore needs to be compensated for satellite motions during the time interval when compared to v_i^e. Several options are available for estimating the average satellite velocity of the interval. Here v_i^e will express the satellite velocity averaged over the beginning and end of the relevant GNSS receiver sample interval.

The "Riccati Solver & Gain Estimator" block considers the choice of gain matrix K for the TMO. In order to compute the injection terms the estimated position and velocity of the rover and base station is fed back from the TMO.

When considering the stability of the observer structure it is advantageous to examine the individual parts of the modular structure. The nonlinear attitude observer was proven to be semi-globally exponentially stable (SGES) with respect to attitude initialization in [28]. Following the results of [27], the equilibrium point of the double-differenced observer proposed in Section VI, is exponentially stable. The complete observer structure will be exponentially stable with a semi-global region of attraction with respect to attitude initialization due to the feedback interconnection and the SGES properties of the attitude estimator. A rigorous stability proof supporting this is given in [46]. The observer position and velocity estimates can be accurately initialized with the procedure proposed in [27].

In the following, the nonlinear attitude observer will be introduced in Section V, while the TMO will be introduced utilizing the double-differenced receiver configuration in Section VI.

V. Nonlinear Attitude Observer

The following section introduces the nonlinear attitude observer. The orientation of the stationary base station is unimportant and only the attitude of the moving rover will be considered.

The attitude of the rover, given as the rotation between Body- and ECEF-frame, is represented as a unit quaternion to avoid singularities at steep pitch angles. A recent attitude observer proposed by [29], [47], [32], is used where addi-

tionally the gyro bias is determined. The nonlinear attitude observer with injection term $\hat{\sigma}$ is introduced as:

$$\dot{\hat{q}}_b^e = \frac{1}{2}\hat{q}_b^e \otimes \left(\overline{\omega}_{ib,\text{IMU}}^b - \overline{\hat{b}}^b + \overline{\hat{\sigma}}\right) - \frac{1}{2}\overline{\omega}_{ie}^e \otimes \hat{q}_b^e, \tag{15}$$

$$\dot{\hat{b}}^b = \text{Proj}(-k_I\hat{\sigma}, \|\hat{b}^b\|_2 \leq M_{\hat{b}}), \tag{16}$$

$$\hat{\sigma} = k_1 \underline{v}_1^b \times R(\hat{q}_b^e)^\intercal \underline{v}_1^e + k_2 \underline{v}_2^b \times R(\hat{q}_b^e)^\intercal \underline{v}_2^e, \tag{17}$$

where $\text{Proj}(\cdot,\cdot)$ describes the projection operator limiting the gyro bias estimate to a sphere with radius $M_{\hat{b}}$ with $M_{\hat{b}} > M_b$. The tuning constants k_1, k_2 and k_I are chosen positive and sufficiently large.

The injection term considers two vectors $\underline{v}_1^b$ and $\underline{v}_2^b$ in the Body-frame and their corresponding vectors $\underline{v}_1^e$ and $\underline{v}_2^e$ in the ECEF-frame. These vectors can be chosen in various ways but will here be based on specific force and magnetic field:

$$\underline{v}_1^b = \frac{f_{\text{IMU}}^b}{\|f_{\text{IMU}}^b\|_2}, \qquad \underline{v}_2^b = \frac{m_{\text{MAG}}^b}{\|m_{\text{MAG}}^b\|_2} \times \underline{v}_1^b,$$
$$\underline{v}_1^e = \frac{\hat{f}^e}{\|\hat{f}^e\|_2}, \qquad \underline{v}_2^e = \frac{m^e}{\|m^e\|_2} \times \underline{v}_1^e,$$

where m^e is the position dependent magnetic field vector of the Earth assumed known for the rover's estimated position and the specific force estimate $\hat{f}^e$ is supplied by the TMO.

An advantage of this attitude observer is the constant gains of the injection term, leading to a lower computational load compared to other estimators where a Kalman filter approach will have a significantly higher load due to the matrix inverse and the additional propagation of a covariance matrix. In [27] a similar nonlinear observer is compared to a Multiplicative Extended Kalman filter (MEKF), where the attitude observer was seen to constitute only around 20% of the computational load of the MEKF attitude part (and around 25% when the entire observer structures were compared).

VI. Double-Difference Nonlinear Observer

Denoting the ith satellite as the reference satellite, the double-differenced measurement errors can be used as injection terms in the proposed translational motion observer:

$$\dot{\hat{p}}_r^e = \hat{v}_r^e + \sum_{j=1}^{m-1}\left(K_j^{p\rho} e_{\rho,ij} + K_j^{p\varphi} e_{\varphi,ij} + K_j^{p\upsilon} e_{\upsilon,ij}\right), \tag{18}$$

$$\begin{aligned}\dot{\hat{v}}_r^e = &-2S(\omega_{ie}^e)\hat{v}_r^e + \hat{f}^e + g^e(\hat{p}_r^e) \\ &+ \sum_{j=1}^{m-1}\left(K_j^{v\rho} e_{\rho,ij} + K_j^{v\varphi} e_{\varphi,ij} + K_j^{v\upsilon} e_{\upsilon,ij}\right),\end{aligned} \tag{19}$$

$$\begin{aligned}\dot{\xi} = &-R(\hat{q}_b^e)S(\hat{\sigma})f_{\text{IMU}}^b \\ &+ \sum_{j=1}^{m-1}\left(K_j^{\xi\rho} e_{\rho,ij} + K_j^{\xi\varphi} e_{\varphi,ij} + K_j^{\xi\upsilon} e_{\upsilon,ij}\right),\end{aligned} \tag{20}$$

$$\hat{f}^e = R(\hat{q}_b^e)f_{\text{IMU}}^b + \xi, \tag{21}$$

$$\dot{\hat{p}}_s^e = \sum_{j=1}^{m-1}\left(K_j^{s\rho} e_{\rho,ij} + K_j^{s\varphi} e_{\varphi,ij} + K_j^{s\upsilon} e_{\upsilon,ij}\right), \tag{22}$$

$$\nabla\Delta\dot{\hat{N}} = \sum_{j=1}^{m-1}\left(K_j^{Np} e_{\rho,ij} + K_j^{N\varphi} e_{\phi,ij} + K_j^{N\upsilon} e_{\upsilon,ij}\right). \tag{23}$$

The gains to be determined, $K_j^{\star\star}$, are considered slowly time-varying. Here the auxiliary term, ξ, is presented in order to determine the estimated specific force in ECEF frame, see (21). The advantage of using double-differenced measurements is that the receiver clock bias is cancelled and can therefore be excluded from estimation, while in single receiver configurations it is included in the state vector, see e.g. [46]. The double-differenced phase ambiguities, $\nabla\Delta\hat{N}$, are represented as a vector with $m-1$ elements described as the difference between the single-differenced ambiguities of the ith and jth satellite, i.e. $\nabla\Delta\hat{N} = \left[\Delta\hat{N}_1 - \Delta\hat{N}_i; \Delta\hat{N}_2 - \Delta\hat{N}_i; \ldots; \Delta\hat{N}_j - \Delta\hat{N}_i\right]$. The ambiguity estimates are propagated by the translational motion observer as real valued estimates and can after some convergence be fixed to integer values, which will be discussed in detail in Section VI-B.

It is desired to include the base station position in the observer estimation, such that the observer does not rely on access to a pre-surveyed position, but can be initialized with a more inaccurate estimate of the base station position.

The structure of the TMO is similar to [31] with additional injection terms based on the carrier phase derived Doppler measurements. The injection terms are the difference between measured and estimated double-differenced satellite signals: $e_{\rho,ij} := \nabla\Delta\rho_{ij} - \nabla\Delta\hat{\rho}_{ij}$, $e_{\varphi,ij} := \lambda(\nabla\Delta\varphi_{ij} - \nabla\Delta\hat{\varphi}_{ij})$ and $e_{\upsilon,ij} := \lambda(\nabla\Delta\upsilon_{ij} - \nabla\Delta\hat{\upsilon}_{ij})$, where the estimated terms are:

$$\nabla\Delta\hat{\rho}_{ij} = \nabla\Delta\hat{\psi}_{ij}, \tag{24}$$

$$\lambda\nabla\Delta\hat{\varphi}_{ij} = \nabla\Delta\hat{\psi}_{ij} - \nabla\Delta\hat{N}_{ij}\lambda, \tag{25}$$

$$\lambda\nabla\Delta\hat{\upsilon}_{ij} = \hat{h}_j^{r\intercal}\left(\hat{v}_r^e - v_j^e\right) - \hat{h}_i^{r\intercal}\left(\hat{v}_r^e - v_i^e\right) + \hat{h}_j^{s\intercal} v_j^e - \hat{h}_i^{s\intercal} v_i^e, \tag{26}$$

and the estimated double-differenced geometric baseline is:

$$\begin{aligned}\nabla\Delta\hat{\psi}_{ij} = &\|\hat{p}_r^e - p_j^e\|_2 - \|\hat{p}_r^e - p_i^e\|_2 - \|\hat{p}_s^e - p_j^e\|_2 \\ &+ \|\hat{p}_s^e - p_i^e\|_2,\end{aligned} \tag{27}$$

with the estimated line-of-sight vectors:

$$\hat{h}_i^r = \frac{\hat{p}_r^e - p_i^e}{\|\hat{p}_r^e - p_i^e\|_2}, \qquad \hat{h}_i^s = \frac{\hat{p}_s^e - p_i^e}{\|\hat{p}_s^e - p_i^e\|_2}. \tag{28}$$

Investigating the observer stability, the error states are introduced as $\tilde{p}_r := p_r^e - \hat{p}_r^e$, $\tilde{v}_r := v_r^e - \hat{v}_r^e$, $\tilde{f} := f^e - \hat{f}^e$, $\tilde{p}_s := p_s^e - \hat{p}_s^e$, and $\nabla\Delta\tilde{N} := \nabla\Delta N - \nabla\Delta\hat{N}$, and the state vector of the error dynamics is defined as; $x = [\tilde{p}_r; \tilde{v}_r; \tilde{f}; \tilde{p}_s; \nabla\Delta\tilde{N}]$. Here a combination of (20) and (21) is used to substitute the state ξ with $\hat{f}^e$, as done in [46].

In order to determine the gains, $K_j^{\star\star}$, the injection terms are linearised with respect to the observer states, see Appendix A:

$$e_{\rho,ij} = C_{\rho,ij}\tilde{x} + \eta_{\rho,ij}, \tag{29}$$

$$e_{\varphi,ij} = C_{\varphi,ij}\tilde{x} + \eta_{\varphi,ij}, \tag{30}$$

$$e_{\upsilon,ij} = C_{\upsilon,ij}\tilde{x} + \eta_{\upsilon,ij}, \tag{31}$$

where $\eta_{\star,ij}$ consists of measurement noise and higher order nonlinear terms, which can be disregarded in the gain selection under the assumption that the TMO is accurately initialized. The row vectors consist of the following elements:

$C_{\rho,ij} = [\hat{h}_{ij}^{r\intercal}, 0, 0, -\hat{h}_{ij}^{s\intercal}, 0]$, $C_{\varphi,ij} = [\hat{h}_{ij}^{r\intercal}, 0, 0, -\hat{h}_{ij}^{s\intercal}, \lambda 1_{i,m-1}]$, and $C_{\upsilon,ij} = [\hat{h}_{v,ij}^{r\intercal}, \hat{h}_{ij}^{r\intercal}, 0, \hat{h}_{ij}^{s\intercal}, 0]$, where $1_{i,m-1}$ is a row of $m-1$ zeros with a 1 as the ith element. The differenced line-of-sight vectors are described by:

$$\hat{h}_{ij}^{r} = \frac{\hat{p}_r^e - p_j^e}{\|\hat{p}_r^e - p_j^e\|_2} - \frac{\hat{p}_r^e - p_i^e}{\|\hat{p}_r^e - p_i^e\|_2}, \tag{32}$$

$$\hat{h}_{ij}^{s} = \frac{\hat{p}_s^e - p_j^e}{\|\hat{p}_s^e - p_j^e\|_2} - \frac{\hat{p}_s^e - p_i^e}{\|\hat{p}_s^e - p_i^e\|_2}, \tag{33}$$

$$\hat{h}_{v,ij}^{r} = \frac{\hat{v}_r^e - v_j^e}{\|\hat{p}_r^e - p_j^e\|_2} - \frac{\hat{v}_r^e - v_i^e}{\|\hat{p}_r^e - p_i^e\|_2}. \tag{34}$$

A time-varying measurement matrix consisting of $3(m-1)$ rows can be defined as; $C := \left[C_{\rho,i1}; \ldots; C_{\rho,i(m-1)}; C_{\varphi,i1}; \ldots; C_{\varphi,i(m-1)}; C_{\upsilon,i1}; \ldots; C_{\upsilon,i(m-1)}\right]$. The C matrix is slowly time-varying as the relative motion of the satellites with respect to the receivers is small due to the large separation.

The error dynamics can be determined as:

$$\dot{\tilde{x}} = (A - KC)\tilde{x} + \theta_1(t,\tilde{x}) + \theta_2(t,\tilde{\chi}) + \theta_3(t,\tilde{x}), \tag{35}$$

Here $\tilde{\chi}$ is the combined error variable $\tilde{\chi} := [\tilde{r}; \tilde{b}]$ consisting of the vector part of the quaternion, $\tilde{r} = r - \hat{r}$, and the gyro bias error. The perturbation terms are described as, [28]: $\theta_1(t,x) := [0; -2S(\omega_{ie}^e)x_2 + (g^e(p_r^e) - g^e(p_r^e - x_1)); 0; 0; 0; 0]$, $\theta_2(t,\tilde{\chi}) := [0; 0; \tilde{d}; 0; 0; 0]$, where:

$$\begin{aligned}\tilde{d} = {} & (I - R(\tilde{q})^\intercal) R(q_b^e)(S(\omega_{ib,\mathrm{IMU}}^b) f_{\mathrm{IMU}}^b + \dot{f}^b) \\ & - S(\omega_{ie}^e)(I - R(\tilde{q})^\intercal) R(q_b^e) f_{\mathrm{IMU}}^b - R(\tilde{q})^\intercal R(q_b^e) S(\tilde{b}) f_{\mathrm{IMU}}^b.\end{aligned}$$

In [28] it is shown that $\|\theta_2(t,\tilde{\chi})\|_2 \leq \gamma_3 \|\tilde{\chi}\|_2$, for some positive γ_3. As in [31] the last perturbation term is a result of the injection term linearisation; $\theta_3(t,x) := K\eta(t,x)$, where $\eta(t,x) := [\eta_{\rho,1}; \ldots; \eta_{\rho,m}; \eta_{\varphi,1}; \ldots; \eta_{\varphi,m}; \eta_{\upsilon,1}; \ldots; \eta_{\upsilon,m}]$.

Remark 4: In [28] and [46], which this paper is based on, a time-scaling factor $\theta \geq 1$ is introduced in the stability proof. The stability results require the tuning parameter θ to be chosen sufficiently high, and [28] even offers conservation bounds. However, it is often advantageous to tune the parameter by trial-and-error, increasing the parameter from its lower bound, see also [48]. It is not necessary to include the the scaling factor here, as the stability follows from the results of the previous papers. Furthermore, the scaling can be chosen at its lower bound, in the implementation, thereby removing its effect on the observer structure.

The gain matrices should be chosen such that the nominal linear time-varying closed loop dynamics $(A - KC)$ is stable, see Section VI-A, where:

$$A = \begin{bmatrix} 0 & I_3 & 0 & 0 & 0 \\ 0 & 0 & I_3 & 0 & 0 \\ 0 & 0 & 0 & 0 & 0 \\ 0 & 0 & 0 & 0 & 0 \\ 0 & 0 & 0 & 0 & 0 \end{bmatrix}, \tag{36}$$

$$K = \begin{bmatrix} K_1^{p\rho} & \ldots & K_{m-1}^{p\rho} & K_1^{p\varphi} & \ldots & K_{m-1}^{p\varphi} & K_1^{p\upsilon} & \ldots & K_{m-1}^{p\upsilon} \\ K_1^{v\rho} & \ldots & K_{m-1}^{v\rho} & K_1^{v\varphi} & \ldots & K_{m-1}^{v\varphi} & K_1^{v\upsilon} & \ldots & K_{m-1}^{v\upsilon} \\ K_1^{\xi\rho} & \ldots & K_{m-1}^{\xi\rho} & K_1^{\xi\varphi} & \ldots & K_{m-1}^{\xi\varphi} & K_1^{\xi\upsilon} & \ldots & K_{m-1}^{\xi\upsilon} \\ K_1^{s\rho} & \ldots & K_{m-1}^{s\rho} & K_1^{s\varphi} & \ldots & K_{m-1}^{s\varphi} & K_1^{s\upsilon} & \ldots & K_{m-1}^{s\upsilon} \\ K_1^{N\rho} & \ldots & K_{m-1}^{N\rho} & K_1^{N\varphi} & \ldots & K_{m-1}^{N\varphi} & K_1^{N\upsilon} & \ldots & K_{m-1}^{N\upsilon} \end{bmatrix}.$$

The observer system (18)–(23) has a semi-globally exponentially stable region of attraction with respect to attitude initialization errors and local exponential stablility with respect to TMO initialization errors, following the results of [46].

Selection of the reference satellite has great impact on the performance of the observer, as errors in the measurements from the reference satellite are propagated to all double-differenced measurements. The reference satellite is therefore often chosen as the satellite with the highest elevation since propagation and multipath errors will generally be the smallest, [49, Section 7.3.4]. Another advantage of choosing the satellite with the highest elevation is that this satellite is less likely to be obstructed, thereby keeping phase-lock with the receiver. If the chosen reference satellite is obstructed, a new reference has to be selected in order to construct new double-differenced measurements.

A. Gain Selection

The following section will investigate the crucial considerations of gain selection in connection to implementation of the observer. The notation of this section will therefore consider discrete time, instead of continuous time used to present the observer structure in the previous sections. The observer should be implemented using discrete time where the sampling can be dictated by the fastest sensor, usually the IMU, to ensure convergence and stability. For details on discretization and implementation of a similar modular observer structure see [48].

The TMO gains can, like in [28], be chosen to be constant, thereby reducing the computational load of the observer. However, better performance can be achieved by considering the gains as time-varying, see e.g. [48]. Several options for gain selection are available while in the following the Riccati equation will be considered. In general, the method for determining the gain matrices will not affect the observer stability as long as K satisfies the conditions imposed by the TMO stability requirements. The method described here is similar to a Kalman filter where the gain is chosen based on the solution of the discrete time-varying Riccati equation:

$$P_{k|k-1} = \Phi P_{k-1|k-1} \Phi^\intercal + Q, \tag{37}$$

$$K_k = P_{k|k-1} C^\intercal \left(C P_{k|k-1} C^\intercal + R\right)^{-1}, \tag{38}$$

$$P_{k|k} = (I - K_k C) P_{k|k-1} (I - K_k C)^\intercal + K_k R K_k^\intercal, \tag{39}$$

where k is the discrete incrementing index and $\Phi = e^{AT}$ is the discrete transition matrix, with the sample rate and system order denoted as T and n, respectively. The dynamics of the TMO is the same as for Kalman filters, and the P, R, and Q matrices may therefore be interpreted as covariance matrices. The error covariance matrix, P, has elements corresponding

to the state vector, and will therefore vary in size when the number of available satellites changes due to the inclusion of the carrier phase ambiguities. The covariance of the ambiguities, P_N, is found as the lower right $m-1 \times m-1$ sub-matrix of P. The gain selection can be tuned by choosing the measurement, R, and state covariance matrices, Q, where it is common to consider them as consisting of the elements pertaining to the covariance of the states or measurements, $\sigma_\star^2$, [1, Section 14.4.2]:

$$Q = \text{diag}\left(\sigma_{p_r}^2, \sigma_{v_r}^2, \sigma_f^2, \sigma_{p_s}^2, Q_{\nabla\Delta N}\right), \tag{40}$$

$$R = \text{blockdiag}\left(R_{\nabla\Delta\rho}, R_{\nabla\Delta\varphi}, R_{\nabla\Delta\upsilon}\right). \tag{41}$$

The diagonal elements of the Q matrix correspond to the state vector elements describing the expected level of noise in the state. Similarly for the R matrix, the diagonal elements correspond to variances of the aiding double-differenced satellite measurements. In [1, Section 9.4.2.4] a time-varying R-matrix is proposed where the coefficients are determined based on the satellite elevation and range acceleration. Here the matrices (40)–(41) are kept constant. Due to the differencing with a reference satellite, $R_{\nabla\Delta\star}$ has correlation elements such that the covariance matrix is not diagonal. The sub-matrices of R are in general given as:

$$R_{\nabla\Delta\star} = \begin{bmatrix} \sigma_{\nabla\Delta\star}^2 & \frac{1}{2}\sigma_{\nabla\Delta\star}^2 & \cdots & \frac{1}{2}\sigma_{\nabla\Delta\star}^2 \\ \frac{1}{2}\sigma_{\nabla\Delta\star}^2 & \sigma_{\nabla\Delta\star}^2 & \cdots & \frac{1}{2}\sigma_{\nabla\Delta\star}^2 \\ \vdots & \vdots & \ddots & \vdots \\ \frac{1}{2}\sigma_{\nabla\Delta\star}^2 & \frac{1}{2}\sigma_{\nabla\Delta\star}^2 & \cdots & \sigma_{\nabla\Delta\star}^2 \end{bmatrix}, \tag{42}$$

where $\star$ is a placeholder for pseudorange, carrier phase or carrier phase derived Doppler measurements. The $Q_{\nabla\Delta N}$ is constructed in a similar way where the diagonal is $\sigma_{\nabla\Delta N}^2$ with the remaining elements being $1/2\sigma_{\nabla\Delta N}^2$.

It is possible to reduce the computational load without jeopardizing the performance significantly by determining the TMO gains on a slower time-scale, as shown in [27]. The observer can be implemented using the corrector-predictor architecture of [50, Section 11.3.4], where the observer estimates are propagated at IMU frequency and corrected at the lower GNSS receiver frequency whenever satellite measurements are available. The gain selection can then be implemented on a third and slower time scale where the gains are updated for every 100-2.000 GNSS correction. This slower time-scale can be chosen since the C matrix is slowly time-varying.

B. Integer Ambiguities

The ambiguities in the double-difference observer are initially considered real valued, however, the precision can be further improved if they are correctly resolved to integers. Several methods for fixing the carrier-phase ambiguity have been proposed. Here the "fix and hold" method from [1] will be used to fix the combined variable $\nabla\Delta\hat{N} := \left[\nabla\Delta\hat{N}_1; \nabla\Delta\hat{N}_2; \ldots; \nabla\Delta\hat{N}_{m-1}\right]$ to integer values.

The initial estimate of the ambiguity vector can be determined as the difference between carrier-phase and pseudo-range measurements, i.e. subtraction of (12) from (13):

$$\nabla\Delta\hat{N} = \frac{1}{\lambda}\left(\nabla\Delta\varphi - \nabla\Delta\rho\right), \tag{43}$$

where $\nabla\Delta\varphi := [\nabla\Delta\varphi_1; \nabla\Delta\varphi_2; \ldots; \nabla\Delta\varphi_{m-1}]$ and $\nabla\Delta\rho := [\nabla\Delta\rho_1; \nabla\Delta\rho_2; \ldots; \nabla\Delta\rho_{m-1}]$ are vectors of combined variables. The initialization offered by (43) can be used when new satellites are introduced to the constellation. Initialization should also be carried out if a satellite is re-introduced after a period of obstruction or loss-of-lock, as the ambiguity will have changed.

The initial ambiguity estimates depend strongly on a good initial position of the rover and base station. As these might be difficult to obtain prior to flight the ambiguities should be iterated by the TMO before trying to fix to integer value, to decrease the risk of fixing to wrong integers. After initialization the ambiguities will therefore be propagated by the TMO as real-valued estimates. The estimate can be tested for convergence to integer values by minimizing, [1]:

$$\Omega = \min_{\nabla\Delta\check{N}\in\mathbb{Z}^{m-1}} \left(\nabla\Delta\check{N} - \nabla\Delta\hat{N}\right)^\intercal P_N^{-1} \left(\nabla\Delta\check{N} - \nabla\Delta\hat{N}\right), \tag{44}$$

where $P_N \in \mathbb{R}^{m-1\times m-1}$ is the covariance matrix of the ambiguities, and $\nabla\Delta\check{N}$ is an integer candidate vector. The candidate vector belongs to the search space of:

$$S := \{\nabla\Delta\check{N} \in \mathbb{Z}^{m-1} | \nabla\Delta\hat{N} - c_r\sigma_N \leq \nabla\Delta\check{N} \leq \nabla\Delta\hat{N} + c_r\sigma_N\},$$

where σ_N is the variance of the ambiguity estimates determined by the diagonal elements of P_N; $\sigma_N = \sqrt{\text{diag}(P_N)}$. The constant c_r denotes the confidence interval, which in the following will be considered as; $c_r = 3.29$ for 99.9% confidence interval, assuming normal distribution.

All possible candidate vectors in the search space is tested to see which minimizes (44). The relation between the smallest and second smallest value of (44), respectively called Ω_1 and Ω_2, is used to determined whether significant convergence to a candidate vector is achieved. Here significant is used in a covariance sense, as the search space depends on the covariance matrix of the ambiguities. The convergence test consists of verifying that the best solution, Ω_1, is sufficiently far from the next best solution:

$$\Omega_2\Omega_1^{-1} \geq t_N, \tag{45}$$

where t_N is a threshold value. If the ratio is larger than the threshold the test is accepted and the ambiguities are fixed to the candidate set corresponding to Ω_1. This test can be carried out at every observer iteration until the ambiguities are fixed. However, the search space, S, will initially be too large to computationally feasibly search through all candidate sets, which encourages the use of methods such as the LAMBDA method to decrease the search space. The Least-squares AMbiguity Decorrelation Adjustment (LAMBDA) method was proposed by [9], [10], [11] and uses a change in variables to transform the confidence interval of the ambiguities to cover a smaller area. The transformation is carried out by use of the decorrelation matrix, Z, see [1,

Appendix G]:

$$\hat{x}_Z = Z\hat{x}_N, \qquad P_Z = ZP_NZ^\intercal, \tag{46}$$

where $\hat{x}_N$ is a collection of the double-differenced ambiguity estimates, i.e. $\hat{x}_N = \nabla\Delta\hat{N}$. The Cholesky factorization is used to determine the decorrelation matrix; $P_N = LDL^\intercal$, where D is a diagonal matrix and L is a lower triangular matrix with unit elements in the diagonal. The decorrelation matrix is then found as; $Z = \lfloor L^{-1} \rceil$, i.e. the rounded inverse of the lower triangular matrix.

After the ambiguity transformation the search space has decreased in size, leaving fewer candidate sets to be tested, making for a faster evaluation. The LAMBDA method is often used in connection with other resolution methods such as the geometry-based approach. Once the ambiguities have been fixed the transformation can be reversed. A key feature of this approach is that due to the rounding operation when determing Z an integer valued x_N corresponds to an integer valued x_Z, and vice versa. Implementation aspects of the LAMBDA method are considered in [51] and [52].

There are two alternatives for handling the fixed ambiguities: a) once the ambiguities are fixed to integer values they are removed from the state vector, decreasing the A, C, K, Q and P matrices in size, or b) the fixed ambiguities are introduced as an additional measurement augmenting the R matrix and the injection terms. The result will be very similar for the two methods. Method a) might be preferred to b) for the decrease in computational power.

According to [53] the residual measurement error should be less than 25% of a wavelength for the integer ambiguity resolution to have high probability of resolving to the correct integer. This implies that with high noise levels in the phase measurements, or uncertainty in the estimated geometric distance the resolution of the ambiguities might lead to the wrong integers resulting in a position error. In the event of loss-of-lock of satellite signals the code measurements can be smoothed by use of the raw Doppler measurements to reduce the convergence time.

VII. Experimental Results

Experimental data from a flight with a fixed-wing Penguin B UAV, see Fig. 4, is used to verify the proposed double-differenced observer structure. The flight was carried out at Eggemoen airport in Norway (60°12′52″N, 10°19′07″E). The UAV was equipped with an ADIS 16488 IMU (with internal magnetometer) collecting acceleration, rotation rate and magnetic field data at 410 Hz, while a u-Blox LEA-6T receiver gathered navigation satellite measurements at 5 Hz coinciding with measurements obtained at a stationary base station at the airport. The base station receiver is of the same brand and type as the rover receiver. The base station additionally logged the ephemeris data required for satellite position and velocity computation. Throughout the flight the baseline is kept under 1 km, such that the assumption of the atmospheric delays experienced by the two receivers are spatially correlated holds.

Fig. 4: Penguin B used for experimental verification.

The sensors (IMU, GNSS receiver and antenna) used are considered low-cost and while even cheaper models are available these are thought to represent the general level of sensors used for UAV flights. The resolution of the sensors and the stability characteristics of the inertial sensors are seen as a limitation on the performance. Better performance can be expected by including better inertial sensors, especially increasing the performance of the navigation solution when GNSS signals are obstructed. Higher grade GNSS receivers might decrease the experienced measurement noise, supply higher C/N_0 ratios and offer higher sample rates. If the measurements are not accurately synchronized errors in the GNSS/INS integration will arise, as investigated in [54]. Here synchronization is achieved with custom printed circuit boards and a PIC32 micro-controller, for details on the highly accurate timing platform see [55].

In the following two versions of the presented observer structure will be investigated where the difference is in the included aiding measurements; Case A uses pseudorange and carrier-phase measurements, while Case B additionally uses the carrier phase derived Doppler measurements. For both cases the inertial measurements are utilized. The structure of Case A was introduced and simulated by the authors in [31].

To ascertain the performance of the proposed observer structure an RTK reference solution is computed using the open source RTKLIB. No cycle slips were present allowing the reference to maintain resolved ambiguities throughout the flight thereby ensuring centimetre level accuracy. The initial 2.3% of the flight has unresolved ambiguities resulting in a reference with decimetre level accuracy, while the remainder of the flight has centimetre level accuracy. The RTK solution is determined from the same GNSS data as is available to the observer implementations. However, the sampling rate of the reference solution will be at GNSS receiver sampling rate while the observer estimates will be at IMU sampling rate. The observer solution will therefore be down-sampled when compared.

The tuning parameters for the Q matrix are chosen as: $Q = \text{blockdiag}\left(0_3\ [m^2], I_3\ [m^2/s^2], 0.00025I_3\ [m^2/s^4],\right.$

$0_3\ [m^2], Q_{\nabla\Delta N}\big)$, where $\sigma_{\nabla\Delta N} = 0.01\ [\lambda^2]$, while the parameters for R are chosen based on the standard deviations of Table I; $\sigma_{\nabla\Delta\rho} = 1.1\ [m^2]$, $\sigma_{\nabla\Delta\varphi} = 0.03\ [m^2]$, and $\sigma_{\nabla\Delta\upsilon} = 0.06\ [m^2/s^2]$ increased to accommodate for bounding Gaussian white noise and higher sample rate as discussed in [1, Section 9.4.2.4]. The pseudorange standard deviation has been decreased compared to Table I to ensure faster convergence. Units have been given in square parenthesis such as not to confuse with variables or constants. The remaining parameters are: $M_b = 0.0087\ [rad^2/s^2]$, $k_1 = 0.8$, $k_2 = 0.2$, $k_I = 0.004$ and $\lambda = 0.1903\ [m]$ corresponding to the GPS L_1 wavelength. The ambiguity threshold is chosen as $t_N = 3$, as suggested by RTKLIB.

The position of the base station is initialized as an average of the receiver position measurements determined over 25 minutes of logged data. This is considered to be sufficiently accurate for this application. However, more accurate initial position estimates will increase the transient performance, encouraging to average over longer periods when possible. Precise Point Positioning (PPP) can ensure a decimetre accurate estimate of the base station, however the drawbacks are long initialization time and access to preceise ephemeris and atmospheric data. The initialization process presented in [46] can be used to initialize the position of the rover and base station, to ensure that the initial positions are close to the true position.

In Fig. 5 the sky plot of the constellation throughout the experiment is shown. The satellite trajectories are marked with individual colors and the last position has been marked with the satellite ID indicating the direction. The reference satellite is chosen to be the SV1 (shown in red) due to the high initial elevation to minimize atmospheric delays. A minimum elevation requirement of 15° is enforced for dismissal of satellites with high propagation errors.

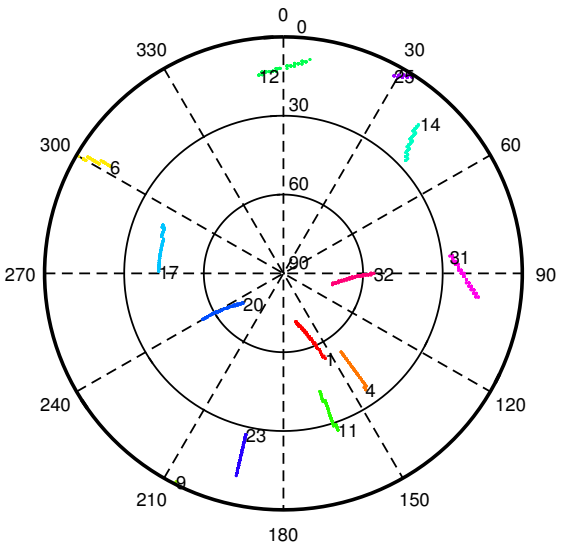

Fig. 5: Sky plot showing elevation and azimuth of satellites. The satellite IDs are included for ease of reference.

The rover GNSS receiver antenna is placed on top of the UAV between the wings. Due to the high dynamics of the flight, with sharp turns the rover looses lock on satellites with low elevation. Only five satellites are considered in the following test to ensure that the integer ambiguities do not require frequent resetting. The satellites to be included are chosen as SV1, SV4, SV11, SV17, SV20, and SV32, which all have high elevation angles. The dilution of precision (DOP) will be large due to the clustering of the used satellites, and higher performance, especially in the vertical component, might be expected when using a broader satellite constellation. Here the constellation can be considered akin to a worst-case scenario with regards to the dilution of precision.

The trajectory of the UAV includes several fast dynamic manoeuvres such as figures-of-eights and circles with radius of approximately 210 m. Some points of interest during the flight will be marked in the subsequent figures; ① denotes take-off, ② notes when the UAV has reached the desired altitude beginning a figure-of-eight flight sequence, at ③ the flight pattern is changed to circles, followed by ④ marking the descent with the reference reverting to lower accuracy making it unfit for further comparison shortly prior to landing. These points of interest will be marked in the following figures for ease of performance comparison throughout the flight. The take-off, initial trajectory and landing were performed with manual control, whereas the figures-of-eight and circles were operated by the autopilot.

The initial part of the trajectory can be seen in Fig. 6 showing the flight path up to ②, while the attitude estimation is shown in Fig. 7 with the points of interest marked. The attitude is shown for both cases and is converted from quaternions to Euler angles describing the rotation from Body to NED-frame for more intuitive understanding. The attitude estimation is similar for both cases considered, which is attributed to the modular observer structure where only the specific force estimate changes with the case. The point of Fig. 7 is not to be able to compare the attitude estimation between the two cases but rather to visualize that there is little difference between the cases. It should be noted that the oscillatory behaviour of the pitch estimate between ③ and ④ corresponds well with the observed behaviour during flight, where a slightly sinusoidal vertical trajectory during the circular flight pattern was present. This was due to an uncompensated issue in the autopilot.

The relative position between rover and base station is determined and compared to the relative position offered by the reference. The relative position estimation errors for the proposed observer can be seen in Fig. 8. It is clear that the integer ambiguities are resolved well in advance of take-off. The transient period of 35 s is not visible in the figure, due to the initial offset. However, the transient behaviour can be seen in Fig. 9. The performance of the position estimates are compared in Table II, where root-mean-square errors (RMSE) and standard deviations (STD) are summarised. The values are determined after the initial transient period of 35 s. An additional test case is included in Table II where the base station position has been excluded from the state vector and is considered constant at the initial position. This test will

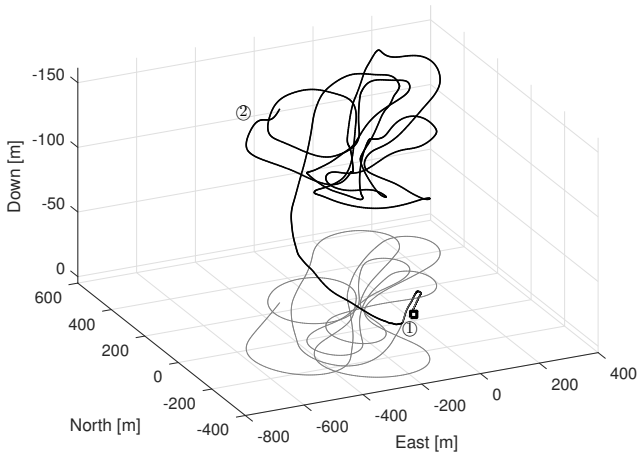

Fig. 6: Initial trajectory of rover (lines), projected ground (grey), and base station (square) during first 400 sec.

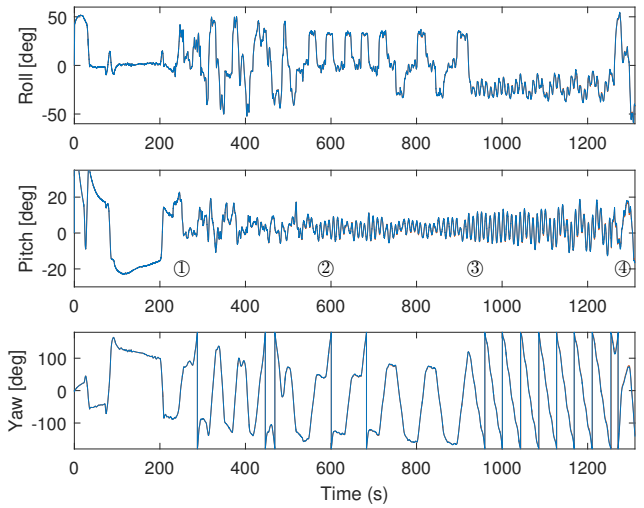

Fig. 7: Rover attitude estimation; Case A (red) and Case B (blue).

be denoted Case C and will utilize pseudorange and carrier-phase aiding. The accuracy obtained by Case C is greatly dependent on the quality of the base station position estimate, while Case A and B estimate the base station position as part of the state vector.

The performance of Case A and Case B are very similar and are not influenced by the dynamics of the flight. Case B might have advantages in velocity estimation, however, as no reliable velocity reference is available this cannot be confirmed. Small drifts are present in the position estimation, e.g. of approximately $1.7 \cdot 10^{-5} m/s$ in North direction.

The fast convergence and high accuracy shown in Fig. 8 are attributed to the ambiguity resolution. In Fig. 10 the ambiguities for Case A are shown for the first 35 s, with similar results obtained for Case B. The real-valued estimate is shown in blue, with the RTKLIB reference integers in black. The rounded estimates are shown in red and only serve as a visual comparison to the reference integers, as the resolved integers are not guaranteed to be the same as

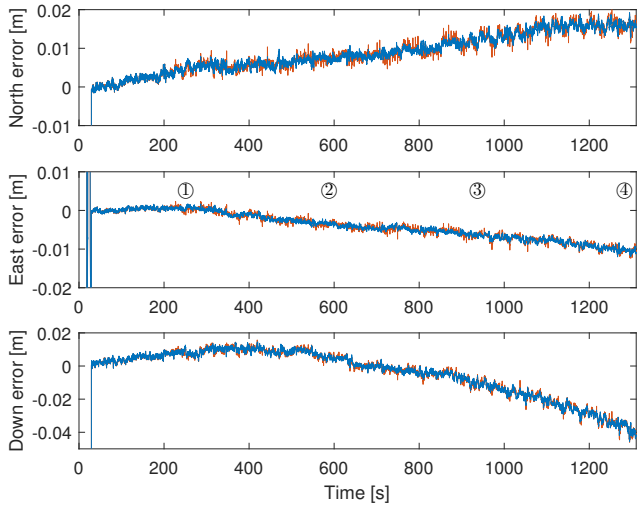

Fig. 8: NED relative position estimation error for Case A (blue) and Case B (red).

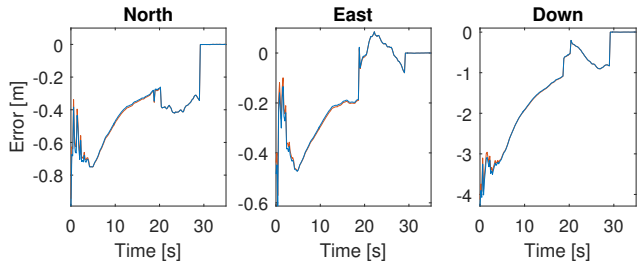

Fig. 9: Transient behaviour of NED relative position estimation error for Case A (blue) and Case B (red).

the rounded real-valued estimates. The estimated ambiguities are seen to quickly converge to the reference value, with one exception for SV17, where the stationary value is one wavelength off. This is considered acceptable and will still give high precision as seen in Fig. 8 and Table II.

TABLE II: Performance comparison of relative NED position estimation error (unit: **centimetre**).

	AIDING			RMSE			STD		
	ρ	φ	υ	N	E	D	N	E	D
Case A:	X	X		1.005	0.534	1.482	0.481	0.343	1.421
Case B:	X	X	X	1.008	0.534	1.485	0.487	0.344	1.423
Case C:	X	X		1.005	0.533	1.482	0.481	0.343	1.421

Looking at Table II the RMSE and standard deviations are seen to be on centimetre-level for all three cases, with sub-centimetre level STD for the horizontal components. The vertical components are seen to be less accurate than the horizontal components for all three cases. This can be attributed in part to the clustered satellite constellation, and the general result of less accurate vertical channel offered by GNSS measurements. Case C has slightly better performance than Case A. However, as the difference is on sub-millimetre level Case A and Case C practically offers the same solution. It is therefore concluded that the inclusion of the base station

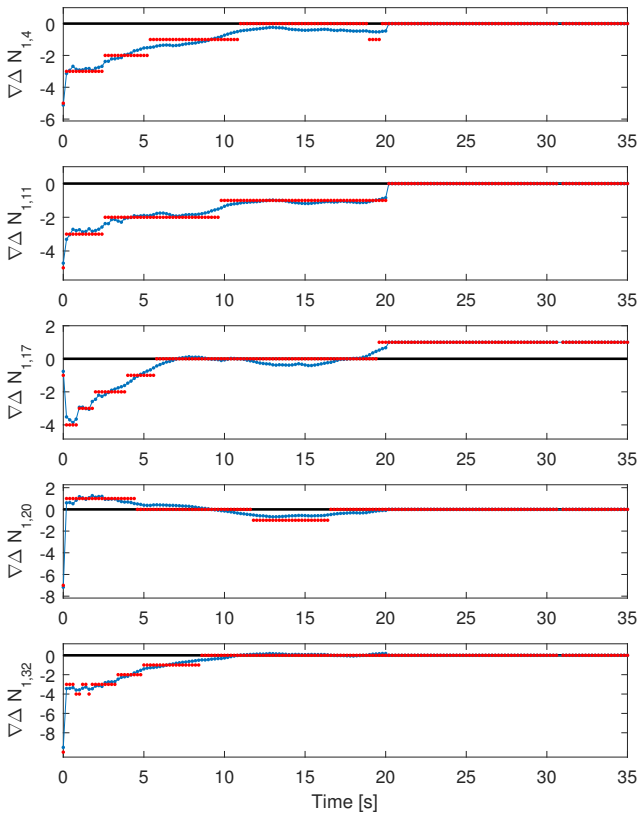

Fig. 10: Example of real-valued ambiguity error of Case A (blue), rounded ambiguities (red), with reference integer (black).

position in the state vector does not lead to poorer state estimates and will be encouraged, especially in case of a slightly moving base station such as a base station on a ship during station keeping, or if a precise initial base station position cannot be obtained. These performance results are considered good in view of the low-cost sensors used and the clustered satellite constellation.

A. Float vs. Fixed Ambiguities

In order to ascertain the influence of the ambiguities a test with only real-valued ambiguities is compared to Case A. This test will be denoted Case D, and will not differ in any way from Case A, apart from the carrier-phase ambiguities being unresolved. In Fig. 11 Case D and Case A are compared.

For Case D the RMSE value is $[1.277; 0.942; 4.399]$ m with standard deviations of $[1.212; 0.865; 1.711]$ m, which is approximately two orders of magnitude larger than with resolved ambiguities. It is clear that for applications with demands of high accuracy the ambiguities need to be resolved, which is expected.

B. Low Elevation Constellation

A low elevation test is carried out to evaluate the performance when using satellites with low elevation angles. This can simulate a high latitude flight close to the poles where the GPS constellation coverage is poor granting only

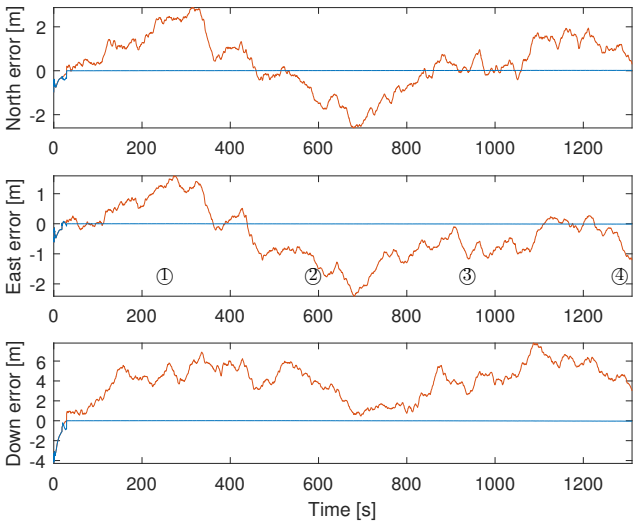

Fig. 11: NED relative position estimation for Case A (blue) and Case D (red).

access to satellites at low elevation. The same data as used in the test above is utilized, here with an elevation mask of 5°. The atmospheric disturbances experienced will differ compared to a high latitude flight, however, this test can give an impression on the possible performance achievable.

In a high latitude, e.g. Arctic, setting the environment would be different from the one considered here where major differences include: a) the terrain in the Arctic will be completely open sky, whereas here some obstruction is caused by trees and mountains, b) the ionospheric and tropospheric conditions, c) different number of satellites, and d) choice of satellites; the best set of satellites based on e.g. DOP and C/N_0 will be selected, whereas here a poor subset of the satellites is chosen.

Satellites with high elevation are masked out. The satellites; SV4, SV6, SV11, SV14, SV23 and SV31 are used, where SV11 has been included to satisfy the $m \geq 4$ assumption, as the low elevation satellites often are obstructed jeopardizing the constellation size assumption. The satellite SV12 is excluded as several cycle slips were detected. The ambiguities estimates are re-initialized if a satellite is re-introduced in the constellation.

The proposed observer without carrier phase derived Doppler aiding (as in Case A above) is tested with the low elevation constellation, where the performance is shown in Fig. 12. Instances when $m < 5$ are marked with vertical grey lines, e.g. at time 1085 seconds. The test is shortened by a approximately 45 seconds, compared to the previous tests, due to extensive loss of low elevation satellites towards the end of the flight.

It is not possible to resolve the ambiguities reliably due to frequent loss of satellite lock and re-introduction of the satellites. This has a clear impact on the performance of the position estimation. The RMSE values are $[2.200; 6.001; 3.961]$ with standard deviations $[0.367; 0.821; 1.909]$, which is significantly larger than the values listed in Table II and for the

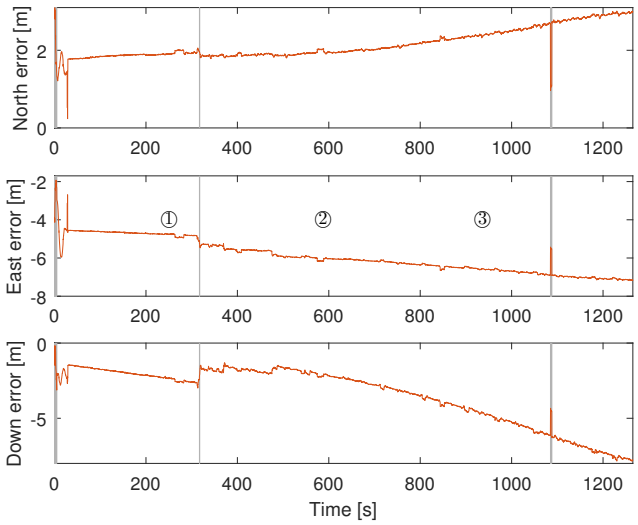

Fig. 12: NED relative position estimation error for Case A using low elevation satellites.

real-valued test in Section VII-A. However, the horizontal accuracy for the rover is seen to be on meter level. This is an improvement over standalone solutions where larger deviations would be expected for a low elevation constellation.

VIII. Concluding Remarks

A tightly-coupled GNSS/INS integration scheme using a dual GNSS-receiver configuration between a stationary base station and a moving rover was proposed where the position and linear velocity of a rover were estimated by a proposed translational motion observer while attitude was determined with a recent nonlinear attitude observer. The proposed translational motion observer utilizes the error of the double-differenced pseudorange, carrier phase and carrier phase derived Doppler satellite measurements between the receivers in the injection terms.

The observer was verified using flight data from an UAV equipped with low-cost sensors, where position estimates were shown to be within 2-4 centimetres of the RTK reference solution throughout a 20 minutes long flight. Convergence of the ambiguities introduced by the carrier-phase measurements was achieved by inclusion in the state vector where they were initially considered real valued later to be resolved to integer values.

Appendix

A. Proof: TMO Injection Terms

The double-differenced injection terms are expressed as:

$$
\begin{aligned}
e_{\rho,ij} &= \|p_r^e - p_j^e\|_2 - \|p_r^e - p_i^e\|_2 - \|p_s^e - p_j^e\|_2 + \|p_s^e - p_i^e\|_2 \\
&\quad - \|\hat{p}_r^e - p_j^e\|_2 + \|\hat{p}_r^e - p_i^e\|_2 + \|\hat{p}_s^e - p_j^e\|_2 - \|\hat{p}_s^e - p_i^e\|_2, \\
e_{\varphi,ij} &= e_{\rho,ij} + \nabla\Delta\tilde{N}_{ij}\lambda, \\
e_{\upsilon,ij} &= \left(h_j^r - h_i^r\right)^\intercal v_r^e - \left(\hat{h}_j^r - \hat{h}_i^r\right)^\intercal \hat{v}_r^e + \left(h_j^s - \hat{h}_j^s\right)^\intercal v_j^e \\
&\quad - \left(h_i^s - \hat{h}_i^s\right)^\intercal v_i^e,
\end{aligned}
$$

Linearisation the injection terms as the first-order Taylor approximation yields:

$$
\begin{aligned}
e_{\rho,ij} &= \left(\frac{\hat{p}_r^e - p_j^e}{\|\hat{p}_r^e - p_j^e\|_2} - \frac{\hat{p}_r^e - p_i^e}{\|\hat{p}_r^e - p_i^e\|_2}\right)^\intercal \tilde{p}_r \\
&\quad - \left(\frac{\hat{p}_s^e - p_j^e}{\|\hat{p}_s^e - p_j^e\|_2} - \frac{\hat{p}_s^e - p_i^e}{\|\hat{p}_s^e - p_i^e\|_2}\right)^\intercal \tilde{p}_s + \eta_{\rho,ij}, \\
e_{\varphi,ij} &= \left(\frac{\hat{p}_r^e - p_j^e}{\|\hat{p}_r^e - p_j^e\|_2} - \frac{\hat{p}_r^e - p_i^e}{\|\hat{p}_r^e - p_i^e\|_2}\right)^\intercal \tilde{p}_r + \lambda\nabla\Delta\tilde{N}_{ij} \\
&\quad - \left(\frac{\hat{p}_s^e - p_j^e}{\|\hat{p}_s^e - p_j^e\|_2} - \frac{\hat{p}_s^e - p_i^e}{\|\hat{p}_s^e - p_i^e\|_2}\right)^\intercal \tilde{p}_s + \eta_{\varphi,ij}, \\
e_{\upsilon,ij} &= \left(\frac{\hat{v}_r^e - v_j^e}{\|\hat{p}_r^e - p_j^e\|_2} - \frac{\hat{v}_r^e - v_i^e}{\|\hat{p}_r^e - p_i^e\|_2}\right)^\intercal \tilde{p}_r \\
&\quad + \left(\frac{\hat{p}_r^e - p_j^e}{\|\hat{p}_r^e - p_j^e\|_2} - \frac{\hat{p}_r^e - p_i^e}{\|\hat{p}_r^e - p_i^e\|_2}\right)^\intercal \tilde{v}_r \\
&\quad + \left(\frac{\hat{p}_s^e - p_j^e}{\|\hat{p}_s^e - p_j^e\|_2} - \frac{\hat{p}_s^e - p_i^e}{\|\hat{p}_s^e - p_i^e\|_2}\right)^\intercal \tilde{p}_s + \eta_{\upsilon,ij},
\end{aligned}
$$

where the higher order terms are limited to:

$$
\begin{aligned}
\eta_{\rho,ij} &= \frac{1}{2}\tilde{p}_r^\intercal\left(\check{H}_j^r - \check{H}_i^r\right)\tilde{p}_r - \frac{1}{2}\tilde{p}_s^\intercal\left(\check{H}_j^s - \check{H}_i^s\right)\tilde{p}_s, \\
\eta_{\varphi,ij} &= \frac{1}{2}\tilde{p}_r^\intercal\left(\check{H}_j^r - \check{H}_i^r\right)\tilde{p}_r - \frac{1}{2}\tilde{p}_s^\intercal\left(\check{H}_j^s - \check{H}_i^s\right)\tilde{p}_s, \\
\eta_{\upsilon,ij} &= \frac{1}{2}[\tilde{p}_r\ \tilde{v}_r]\begin{bmatrix} \check{J}_j - \check{J}_i & \check{H}_j^r - \check{H}_i^r \\ \check{H}_j^r - \check{H}_i^r & 0 \end{bmatrix}\begin{bmatrix} \tilde{p}_r \\ \tilde{v}_r \end{bmatrix} \\
&\quad + \frac{1}{2}\tilde{p}_s^\intercal\left(\check{H}_j^s - \check{H}_i^s\right)\tilde{p}_s,
\end{aligned}
$$

for some point $\check{p}_r^e$ between p_r^e and $\hat{p}_r^e$ and:

$$
\begin{aligned}
\check{H}_\star^r &= \frac{1}{\check{\psi}_{r,\star}}I_3 - \frac{(\check{p}_r^e - p_\star^e)(\check{p}_r^e - p_\star^e)^\intercal}{\check{\psi}_{r,\star}^3}, \\
\check{J}_\star &= \frac{1}{\check{\psi}_{r,\star}^3}\left((\check{p}_r^e - p_\star^e)(\check{v}_r^e - v_\star^e)^\intercal + (\check{p}_r^e - p_\star^e)^\intercal(\check{v}_r^e - v_\star^e)I_3\right) \\
&\quad - \frac{3}{\check{\psi}_{r,\star}^5}(\check{p}_r^e - p_\star^e)(\check{p}_r^e - p_\star^e)^\intercal(\check{p}_r^e - p_\star^e)(\check{v}_r^e - v_\star^e),
\end{aligned}
$$

with $\check{\psi}_{r,\star} := \|\check{p}_r^e - p_\star^e\|_2$, where $\star$ is a placeholder for i or j. Similar expressions can be found for $\check{H}_\star^s$ and $\check{\psi}_{s,\star}$ by substitution of r with s. The higher order terms can be bounded, as shown in [46]:

$$
\begin{aligned}
\|\eta_{\rho,ij}\|_2 &\le \check{\psi}_r\|\tilde{p}_r\|_2^2 - \check{\psi}_s\|\tilde{p}_s\|_2^2, \\
\|\eta_{\varphi,ij}\|_2 &\le \check{\psi}_r\|\tilde{p}_r\|_2^2 - \check{\psi}_s\|\tilde{p}_s\|_2^2, \\
\|\eta_{\upsilon,ij}\|_2 &\le \check{\psi}_r\|\tilde{p}_r\|_2\cdot\|\tilde{v}_r\|_2 + \frac{3}{2}\check{\psi}_{r^2}\underline{v}\|\tilde{p}_r\|_2^2 + \check{\psi}_s\|\tilde{p}_s\|_2^2,
\end{aligned}
$$

where:

$$
\check{\psi}_r = \frac{\underline{\psi}_{r,j} - \underline{\psi}_{r,i}}{\underline{\psi}_{r,i}\underline{\psi}_{r,j}}, \quad \check{\psi}_{r^2} = \frac{\underline{\psi}_{r,j}^2 - \underline{\psi}_{r,i}^2}{\underline{\psi}_{r,i}^2\underline{\psi}_{r,j}^2}, \quad \check{\psi}_s = \frac{\underline{\psi}_{s,j} - \underline{\psi}_{s,i}}{\underline{\psi}_{s,i}\underline{\psi}_{s,j}}.
$$

with $\underline{\psi}_{r,i}$ and $\underline{\psi}_{s,i}$ being the lower bounds on the geometric distance between receiver and ith satellite, and $\|v_r^e - v_i^e\|_2 \le \underline{v}$.

ACKNOWLEDGMENT

This work was supported by the Norwegian Research Council (projects no. 221666 and 223254) through the Centre of Autonomous Marine Operations and Systems at the Norwegian University of Science and Technology, NTNU.

The authors are grateful for the assistance provided by the UAV engineers at NTNU and Maritime Robotics AS, in particular Lars Semb and Carl Erik Stephansen. Significant contributions to the construction of the UAV payload was made by the rest of the team at NTNU, in particular Sigurd Albrektsen.

REFERENCES

[1] P. D. Groves, *Principles of GNSS, Inertial, and Multisensor Integrated Navigation Systems*. Artech House, 2013.

[2] J. A. Farrell, *Aided Navigation: GPS with High Rate Sensors*. McGraw Hill, 2008.

[3] M. George and S. Sukkarieh, "Tightly Coupled INS/GPS With Bias Estimation for UAV Application," *Proceedings of Australiasian Conference on Robotics and Automation (ACRA)*, vol. -, pp. –, 2005.

[4] Y. Li, J. Wang, C. Rizos, P. Mumford, and W. Ding, "Low-Cost Tightly Coupled GPS/INS Integration Based on a Nonlinear Kalman Filtering Design," *ION*, 2006.

[5] D. A. Grejner-Brzezinska, R. Da, and C. Toth, "GPS Error Modeling and OTF Ambiguity Resolution for High-Accuracy GPS/INS Integrated System," *Journal of Geodesy*, vol. Vol. 72, pp. 626–638, 1998.

[6] J. D. Gautier and B. W. Parkinson, "Using the GPS/INS Generalized Evaluation Tool (GIGET) for the Comparison of Loosely Coupled, Tightly Coupled and Ultra-Tightly Coupled Integrated Navigation Systems," *Proc. ION CIGTF*, pp. 65–76, 2003.

[7] D. Grejner-Brzezinska and C. K. Toth, "Performance Study of High-End Dual Frequency GPS Receivers Tightly Integrated with a Strapdown INS," *Proc. 3rd International Symposium on Mobile Mappig*, 2001.

[8] R. Hirokawa and T. Ebinuma, "A Low-Cost Tightly Coupled GPS/INS for Small UAVs Augmented with Multiple GPS Antennas," *Navigation: JION*, vol. Vol. 56, No. 1, pp. 35–44, 2009.

[9] P. J. G. Teunissen, "The Least-Squares Ambiguity Decorrelation Adjustment: A Method for Fast GPS Integer Ambiguity Estimation," *Journal of Geodesy*, vol. 70, pp. 65–82, 1995.

[10] P. J. G. Teunissen., P. J. de Jonge, and C. C. J. M. Tiberius, "The LAMBDA-Method for Fast GPS Surveying," *GPS Technology Applications, international sympositum*, vol. -, pp. 1–8, 1995.

[11] P. J. G. Teunissen, P. J. de Jonge, and C. C. J. M. Tiberius, "The Volume of the GPS Ambiguity Search Space and its Relevance for Integer Ambiguity Resolution," *ION GPS 1996*, vol. -, pp. 889 – 898, 1996.

[12] Y. Chen, S. Zhao, and J. A. Farrell, "Computationally Efficient Carrier Integer Ambiguity Resolution in Multiepoch GPS/INS: A Common-Position-Shift Approach," *IEEE Transactions on Control Systems Technology*, pp. 1–16, 2015.

[13] A. Chen, D. Zheng, A. Ramanandan, and J. A. Farrell, "INS Aided GPS Integer Ambiguity Resolution," *IEEE International Conference on Control Applications (CCA), Part of 2011 IEEE Multi-Conference on Systems and Control.*, vol. -, pp. 567–572, 2011.

[14] A. Chen, D. Zheng, A. Ramanandan, and J. A. Farrell, "Near-real-time GPS Integer Ambiguity Resolution," *IEEE Conference on Decision and Control and European Control Conference*, pp. 7281–7286, 2011.

[15] T. Takasu and A. Yasuda, "Evaluation of RTK-GPS Performance with Low-cost Single-frequency GPS Receivers," *Proceedings of international symposium on GPS/GNSS*, 2008.

[16] T. Takasu and A. Yasuda, "Development of the Low-cost RTK-GPS Receiver with an Open Source Program Package RTKLIB," *International Symposium on GPS/GNSS*, 2009.

[17] M. Bahrami and M. Zeibart, "Doppler-Aided Positioning - Improving Single-Frequency RTK in the Urban Environment," *GPS World - Innovation, Algorithms and Methods*, vol. May, pp. 47–56, 2011.

[18] S. Miura, L.-T. Hsu, F. Chen, and S. Kamijo, "GPS Error Correction With Pseudorange Evaluation Using Three-Dimensional Map," *IEEE Trans. on Intelligent Transportation Systems*, vol. Vol. 16, No. 6, pp. 3104–3115, 2015.

[19] J. Wendel, O. Meister, R. Mönikes, and G. F. Trommer, "Time-Difference Carrier Phase Measurements for Tightly Coupled GPS/INS Integration," *IEEE/ION Position, Location, and Navigation Symposium*, 2016.

[20] R. M. Watson, V. Sivaneri, and J. N. Gross, "Performance Characterization of Tightly-Coupled GNSS Precise Point Positioning Inertial Navigation wiwith a Simulation Environment," *AIAA Guidance, Navigation, and Control Conference*, pp. 1–18, 2016.

[21] J. A. Farrell, T. D. Givargis, and M. J. Barth, "Real-Time Differential Carrier Phase GPS-Aided INS," *IEEE Transactions on Control Systems Technology*, vol. 8, 4, pp. 709–720, 2000.

[22] M. Dorn, J. O. Filwarny, and M. Wieser, "Inertially-Aided RTK Based on Tightly-Coupled Integration Using Low-Cost GNSS Receivers," *European Navigation Conference*, 2017.

[23] P. Batista, "Long Baseline Navigation With Clock Offset Estimation and Discrete-Time Measurements," *Control Engineering Practice*, vol. 35, pp. 43–53, 2015.

[24] P. Batista, "GES Long Baseline Navigation With Unkown Sound Velocity and Discrete-Time Range Measurements," *IEEE Transactions on Control Systems Technology*, vol. 23, pp. 219–230, 2015.

[25] P. Batista, C. Silvestre, and P. Oliveira, "Single Range Aided Navigation and Source LocalizLocal: Observability and Filter Design," *Systems and Control Letters*, vol. 60, pp. 665–673, 2011.

[26] P. Batista, C. Silvestre, and P. Oliveira, "Tightly Coupled Long Baseline/Ultra-Short Baseline Integrated Navigation System," *International Journal of Systems Science*, pp. 1–19, 2014.

[27] T. A. Johansen, J. M. Hansen, and T. I. Fossen, "Nonlinear Observer for Tightly Integrated Inertial Navigation Aided by Pseudo-Range Measurements," *ASME J. Dynamic Systems, Measurement and Control*, vol. Vol. 139, Paper DS-15-1088, 2017; DOI 10.1115/1.4034496, 2017.

[28] H. F. Grip, T. I. Fossen, T. A. Johansen, and A. Saberi, "Nonlinear Observer for GNSS-Aided Inertial Navigation with Quaternion-Based Attitude Estimation," *American Control Conference*, vol. -, pp. 272–279, 2013.

[29] R. Mahony, T. Hamel, and J.-M. Pflimlin, "Nonlinear Complementary Filters on the Special Orthogonal Group," *IEEE Transactions on Automatic Control*, vol. 53, No 5, pp. 1203–1218, 2008.

[30] M.-D. Hua, "Attitude Estimation for Accelerated Vehicles using GPS/INS Measurements," *Control Engineering Practice*, vol. 18, pp. 723–732, 2010.

[31] J. M. Hansen, T. A. Johansen, and T. I. Fossen, "Tightly Coupled Integrated Inertial and Real-Time-Kinematic Poisitioning Approach Using Nonlinear Observer," *American Control Conference, Boston*, pp. pp. 5511–5518, 2016.

[32] H. F. Grip, T. I. Fossen, T. A. Johansen, and A. Saberi, "Attitude Estimation Using Biased Gyro and Vector Measurements With Time-Varying Reference Vectors," *IEEE Transactions on Automatic Control*, vol. 57, pp. 1332–1338, 2012.

[33] H. F. Grip, T. I. Fossen, T. A. Johansen, and A. Saberi, "Nonlinear Observer for Attitude, Position and Velocity: Theory and Experiments," *Chapter 17 in "Multisensor Attitude Estimation" (H. Fourati and D. C. Belkhia, Eds.), CRC Press (Taylor & Francis Group)*, pp. 291–314, 2016.

[34] L. Serrano, D. Kim, and R. B. Langley, "A Single GPS Receiver as a Real-Time, Accurate Velocity and Acceleration Sensor," *Proceedings of the the 17th International Technical Meeting of the Satellite Division of The Institute of Navigation (ION GNSS 2004), Long Beach, CA, USA*, vol. 2124, 2004.

[35] S. Moafipoor, D. A. Grejner-Brzezinska, and C. K. Toth, "Tightly Coupled GPS/INS Integration Based on GPS Carrier Phase Velocity Update," *ION NTM*, vol. -, pp. –, 2004.

[36] M. Petovello, "The Differences in Differencing," *Inside GNSS - GNSS Solutions*, vol. September/October, pp. 28–32, 2011.

[37] R. W. Beard and T. W. McLain, *Small Unmanned Aircraft - Theory and Practice*. Princeton University Press, 2012.

[38] C. Goad and L. Goodman, "Modified Hopfield Tropospheric Refraction Correction Model," *Transations - American Geophysical Union*, vol. Vol. 55, 1974.

[39] F. Niu, Y. Morton, J. Wang, and W. Pelgrum, "GPS Carrier Phase Detrending Methods and Performances for Ionosphere Scintillation Studies," *International Technical Meeting of The Insitute of Navigation*, 2012.

[40] S. C. Mushini, P. T. Jayachandran, R. B. Langley, J. W. MacDougall, and D. Pokhotelov, "Improved Amplitude- and Phase-scintillation indices derived from Wave Detrended High-latitude GPS Data," *GPS Solution*, vol. Vol. 16, pp. p. 363–373, 2012.

[41] C. J. Benton and C. N. Mitchell, "Isolating the Multipath Component in GNSS Signal-to-Noise Data and Locating Reflecting Objects," *Radio Science*, vol. Vol. 46, pp. 1–11, 2011.

[42] P. F. de Bakker, H. van der Marel, and C. C. J. M. Tiberius, "Geometry-Free Undifferenced, Single and Double Differenced Analysis of Single Frequency GPS, EGNOS and GIOVE-A/B Measurements," *GPS Solution*, vol. 13, pp. 305–314, 2009.

[43] P. F. de Bakker, C. C. J. M. Tiberius, H. van der Marel, and R. J. P. van Bree, "Short and Zero Baseline Analysis of GPS L1 C/A, L5Q, GIOVE E1B, and E5aQ Signals," *GPS Solution*, vol. 16, pp. 53–64, 2012.

[44] B. DeCleene, "Defining Pseudorange Integrity-Overbounding," *Proc. 13th International Technical Meeting of the Satellite Division of the Institute of Navigation*, 2000.

[45] T. Dautermann, C. Mayer, F. Antreich, A. Konovaltsev, B. Belabbas, and U. Kälberer, "Non-Gaussian Error Modeling for GBAS Integrity Assessment," *IEEE Transactions on Aerospace and Electronic Systems*, vol. Vol. 48, pp. 693–706, 2012.

[46] T. A. Johansen and T. I. Fossen, "Nonlinear Observer for Inertial Navigation Aided by Pseudo-Range and Range-Rate Measurements," *European Control Conference*, 2015.

[47] H. F. Grip, T. I. Fossen, T. A. Johansen, and A. Saberi, "A Nonlinear Observer for Integration of GNSS and IMU Measurements with Gyro Bias Estimation," *Proceedings of the American Control Conference*, 2012.

[48] T. H. Bryne, J. M. Hansen, R. H. Rogne, N. Sokolova, T. I. Fossen, and T. A. Johansen, "Nonlinear Observers for Integrated INS/GNSS Navigation - Implementation Aspects," *IEEE Control Systems Magazine*, vol. 37, No. 3, pp. 59 – 86, 2017.

[49] P. Misra and P. Enge, *Global Positioning System - Signals, Measurements, and Performance*. Ganga-Jamuna Press, 2006.

[50] T. I. Fossen, *Handbook of Marine Craft Hydrodynamics and Motion Control*. John Wiley & Sons, Ltd, 2011.

[51] P. de Jonge and C. Tiberius, "The LAMBDA Method for Integer Ambiguity Estimation: Implementation Aspects," *Publications of the Delft Geodetic Computing Centre, LGR-Series*, vol. -, pp. –, 1996.

[52] P. Joosten and C. Tiberius, "LAMBDA: FAQs," *GPS Solutions*, vol. 6, pp. 109–114, 2002.

[53] M. G. Petovello, S. Feng, and W. Ochieng, "How do you Trust Centimeter Level Accuracy Positioning?" *Inside GNSS - GNSS Solutions*, vol. September/October, 2014.

[54] J. M. Hansen, T. I. Fossen, and T. A. Johansen, "Nonlinear Observer Design for GNSS-Aided Inertial Navigation Systems with TIme-Delayed GNSS Measurements," *Control Engineering Practice*, vol. (to appear), 2017.

[55] S. M. Albrektsen and T. A. Johansen, "SyncBoard - A high accuracy sensor timing board for UAV payloads," *International Conference on Unmanned Aircraft Systems*, 2017.